Comptes Rendus

Mécanique

Malo Valmalle, Montcho Crépin Hounlonon, Benjamin Smaniotto, Clément A. Kouchadé and François Hild

Digital Volume Correlation analyses to study deformation and damage mechanisms of teak in torsion

Digital Volume Correlation analyses to study deformation and damage mechanisms of teak in torsion

Malo Valmalle [a]**, Montcho Crépin Hounlonon** ⊕ [b]**, Benjamin Smaniotto** [a, c]**,**
Clément A. Kouchadé ⊕ [b] **and François Hild** ⊕ *, [c]

[a] ENS Paris-Saclay, DER Génie Mécanique, Gif-sur-Yvette, France

[b] Université d'Abomey-Calavi (UAC), Faculté des Sciences et Techniques (FAST),
Laboratoire de Physique du Rayonnement (LPR), Abomey-Calavi, Bénin

[c] Université Paris-Saclay, CentraleSupélec, ENS Paris-Saclay, CNRS,
LMPS–Laboratoire de Mécanique Paris-Saclay, Gif-sur-Yvette, France

E-mails: malo.valmalle@ens-paris-saclay.fr (M. Valmalle), shortreckno@yahoo.fr
(M. C. Hounlonon), benjamin.smaniotto@ens-paris-saclay.fr (B. Smaniotto),
ckouchade@yahoo.fr (C. A. Kouchadé), francois.hild@ens-paris-saclay.fr (F. Hild)

Abstract. Wood is a material with anisotropic elastic properties at the macroscale. In the present work, a sample made of Beninise teak was subjected to *in situ* torsion. Digital Volume Correlation (DVC) analyses were run at the mesoscale to measure displacement fields. The corresponding strain fields were obtained at the same scale in addition to the gray level residuals at the voxel scale. The out-of-plane shear modulus could be calibrated at the macroscale and was in good agreement with earlier results of the coauthors (MCH and CAK). The ultimate shear strength was also assessed at the same scale. Last, damage was detected and quantified at the mesoscale thanks to strain fields and at the microscale via gray level residual fields.

Keywords. Crack, Digital Volume Correlation (DVC), *In situ* test, Tomography, Wood.

1. Introduction

Teak (*Tectona grandis* L. f.) is a tropical wood that is used very extensively [1], for instance in shipbuilding, carpentry, cabinet making, flooring, stairs, frameworks, garden furniture, railway sleepers, bridges and other constructions in contact with water [2]. Because of all these uses, teak wood remains one of the most in demand timber species in the international market and hence calls for reliable knowledge of its mechanical properties.

---

* Corresponding author.

The determination of mechanical properties of wood is standardized and usually requires mechanical tests to be performed at the macroscopic scale [3–8]. Alternative routes are followed by resorting, for instance, to acoustic, vibroacoustic, ultrasonic, or vibrational techniques [9]. Even though some specific geometry has been proposed to quantify the shear strength of wood [10], there is no consensus on their extraction [11, 12]. All the above-mentioned analyses were performed on teak samples whose transverse dimensions were centimetric and reported the modulus of elasticity (i.e., Young's modulus); none of them assessed a shear modulus. Further, the mechanical properties of wood, in particular teak [8], are influenced by moisture content, density, age, position in the tree trunk, temperature, origin, species, heredity [13–17] to cite a few factors.

In order to increase the value of Beninese teak production, the Radiation Physics Laboratory has undertaken extensive research into its physical and mechanical characterization. Mechanical tests made it possible to discriminate between plantations whose seeds were of local and Tanzanian origins [1]. The present study allows these results to be refined through a more precise analysis, in particular the evaluation of the out-of-plane shear stiffness and strength of teak, which remain difficult to determine [12]. The latter was assessed with an *in situ* torsion test on a rectangular cuboid. Further, damage was also studied at three different scales. The test reported hereafter was monitored via Digital Volume Correlation (DVC).

DVC analyses were first reported to quantify the deformation of wood in *in situ* flexural tests when monitored via micro-computed tomography [18, 19]. In these first cases, so-called local registrations were performed at a 0.1 mm scale for a millimetric sample. The compressive behavior of fibrous material composed of wood fibers could also be investigated thanks to local DVC analyses performed at the sub-millimeter scale [20]. As for Digital Image Correlation (DIC), there are essentially two types of approaches to measure volumetric displacements [21], namely, local DVC in which small and independent sub-volumes are registered [22, 23] and global (or FE-based) DVC [24, 25] for which the whole region of interest is meshed and correlated in a single analysis. Global DVC was utilized to assess swelling of spruce wood from dry to wet humidity states with 27 μm elements [26]. Indentation tests on Norway spruce were also studied with such approach with elements of the order of 130 μm in length [27]. To the best of the authors' knowledge, no *in situ* torsion test has so far been reported for wood.

The outline of the paper is as follows. First, the *in situ* torsion experiment is presented. Then, the different steps of the DVC approach are introduced. In the present study, global DVC was used. The measured displacement fields, as well as corresponding strain and residuals fields, are analyzed to detect and quantify damage. The ultimate torsional strength in addition to the out-of-plane shear modulus were also extracted from the measured data.

2. *In situ* torsion test

The samples used herein were made of 23-year old teak wood from the National Timber Office of Benin (ONAB) plantation of Djigbé. Their dimensions in the reference Radial, Tangential and Longitudinal (R, T, L) directions (corresponding to the x, y, z axes) were $19.8 \times 19.4 \times 100$ mm. Such dimensions are consistent with previous studies on the extraction of macroscopic properties of teak [1, 4–7]. The specimens were machined from the same piece of heartwood cut at human height. Figure 1(a) shows a 3D rendering of the central part of the sample that was imaged via X-ray tomography. The longitudinal section (Figure 1(b)) reveals the fibrous mesostructure of teak. The transverse section exhibits radial growth with different layers (i.e., rings).

The *in situ* torsion test was monitored using computed microtomography [28]. Such imaging technique is non-intrusive and provides 3D images of the sample tested *in situ* [29]. Conversely, it usually requires rather long scan durations that may become problematic when the material
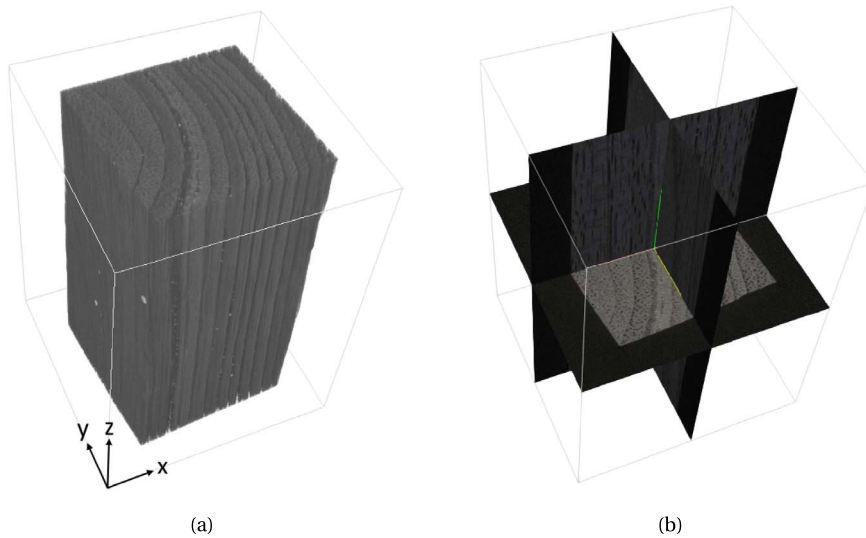
Figure 1. (a) 3D rendering of the studied teak sample (size of displayed teak volume: 19.8 × 19.4 × 40 mm). (b) Corresponding orthoslices.
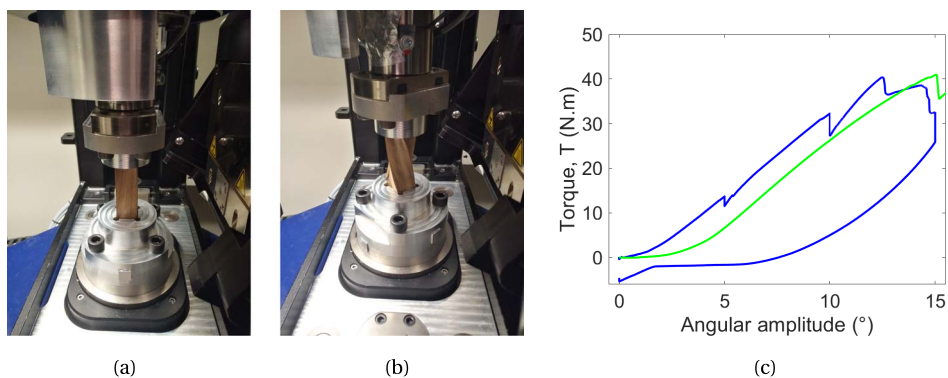

Figure 2. (a) Sample in the reference configuration within the *in situ* testing machine. (b) Deformed configuration after the continuous test. (c) Applied torque vs. angular amplitude for the continuous (green) and *in situ* (blue) tests.

experiences time-dependent phenomena. In the present case, the scan duration was limited to ca. 14 min (see Table 1). Special aluminum alloy grips were designed to load the sample in torsion (Figure 2(a)). Such geometry is close to that proposed by Schwab *et al.* [30]. The samples were mounted tight in the grips. Consequently, friction occurred between the lateral faces.

Prior to the *in situ* test, a continuous test was carried out to select the load levels for which the *in situ* test would be interrupted. The torsion torque was applied by the two angular actuators of the *in situ* testing machine, both controlled in angular position. The angular speed was equal to ±0.1°/s during the loading phases. The test was conducted up to the first signs of damage (Figure 2(b)), which led to the first major load drop (Figure 2(c)). In terms of overall response, the two tested samples led to similar trends apart from the very beginning of the experiment, which was due to the initial settling of the sample in the grips. In particular, the ultimate torque was equal to 40.1 N·m for the continuous test in comparison to 40.5 N·m for the *in situ* experiment.

Table 1. DVC hardware parameters

Tomograph	North Star Imaging X50+
X-ray source	XRayWorX XWT-240-CT
Target/Anode	W (reflection mode)
Filter	None
Voltage	170 kV
Current	120 μA
Focal spot size	5 μm
Tube to detector	333 mm
Tube to object	94 mm
Detector	Dexela 2923
Definition	1536 × 1944 pixels (2 × 2 binning)
Number of projections	900
Angular amplitude	360°
Frame average	5 per projection
Frame rate	20 fps
Acquisition duration	14 min 07 s
Reconstruction algorithm	Filtered back-projection
Gray Levels amplitude	16 bits
Volume size	693 × 695 × 933 voxels (after crop)
Field of view	29.8 × 29.9 × 40.1 mm^3 (after crop)
Image scale	43 μm/voxel
Pattern size (vx)	4/4/50 (Figure 1)

In the present case, reproducible results were obtained up to the ultimate torque even though the conditions were different (i.e., continuous vs. interrupted tests).

For the *in situ* test, the levels of torque and axial force were regularly recorded (Figure 3). The relaxations (in red) at constant angular amplitude correspond to scan acquisitions (Figure 3(a)). They remained very limited thanks to 5-min dwell time between the end of each loading step and the beginning of scanning. Damage inception led to two additional load drops. Given the amplitude of the force fluctuations during scans (Figure 3(b)) and the type of grips used herein (Figure 2), it was difficult to conclude on the presence of a Poynting effect [31] using these load data.

Five scans were performed, namely, two in the reference configuration for uncertainty quantification, and three in the deformed configurations (Figure 3). A series of 900 radiographs per scan were acquired to reconstruct 3D images of the sample (Figure 4) via filtered back-projection [32]. Each scan was acquired between a loading phase during which the angular position of the top grip was increased by 2.5° increments, and the bottom grip by −2.5° increments. The torsion test was stopped for an angular amplitude of 15° between the bottom and top grips, because the torque level dropped significantly (Figure 3(a)), which was a macroscopic signature of damage within the sample.

The hardware parameters of the *in situ* imaging setup are gathered in Table 1. Once cropped, the reconstructed volumes covered 29.79 × 29.88 × 40.12 mm^3 with a 43 μm/vx resolution. It is worth noting that the imaged material did not have an isotropic microstructure (Figure 1). As a consequence, its characteristic lengths measured as the full width at half maximum of its autocorrelation was equal to 4 vx in both in-plane (i.e., x, y) directions, and 50 vx in the longitudinal (i.e., z) direction. The characteristic size of the microstructure was thus two orders
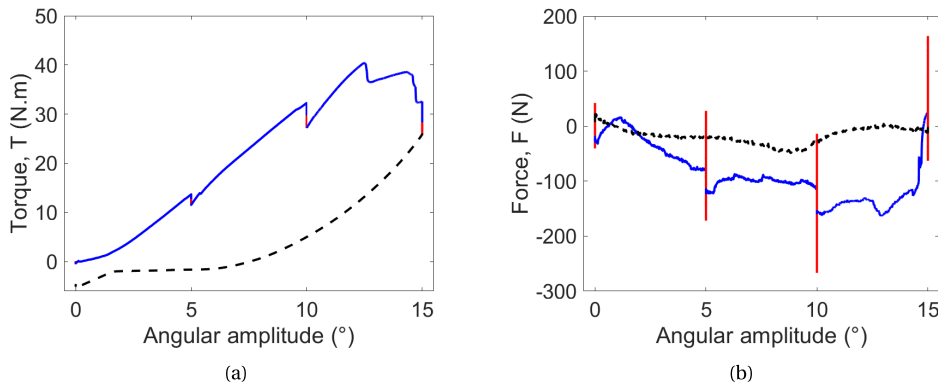
Figure 3. Applied torque (a) and induced normal force (b) of the *in situ* torsion test. The data in red correspond to scan acquisitions, and the black dashed curves to sample unloading.
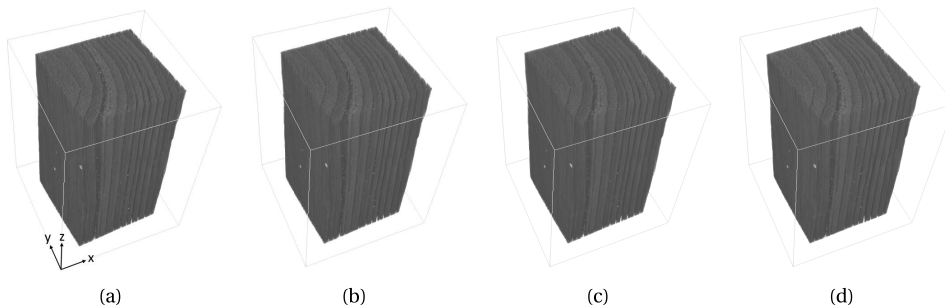

Figure 4. 3D renderings of the reference configuration (a) and the three deformed configurations with angular amplitudes equal to 5° (b), 10° (c), and 15° (d).

of magnitude lower than the investigated volume. Further, the studied height was equal to 20 times the characteristic length. As a consequence, the sought out-of-plane shear modulus is representative of the macroscopic behavior of such material.

3. Different DVC steps

3.1. *Mesh of the reference configuration*

FE-based DVC [24] was used in the present analyses. Such an approach requires an FE mesh to be constructed. Figure 5 shows the considered mesh made of 4-noded tetrahedra (T4). It contained 2000 nodes and 9234 T4 elements whose mean size (measured as the cube root of the average elementary volume) was 28 vx (or ≈1.2 mm). The spatial resolution, which is defined as the cube root of the mean number of voxels utilized to measure nodal displacements, was equal to 46 vx (or ≈2 mm).

As the teak sample was slightly warped by the cutting process, and the frame of the reconstructed volume was slightly rotated with respect to that of the nominal configuration, a preliminary DVC analysis was conducted between the voxelized twin and the reference configuration to backtrack the mesh that was constructed on the nominal geometry [33].
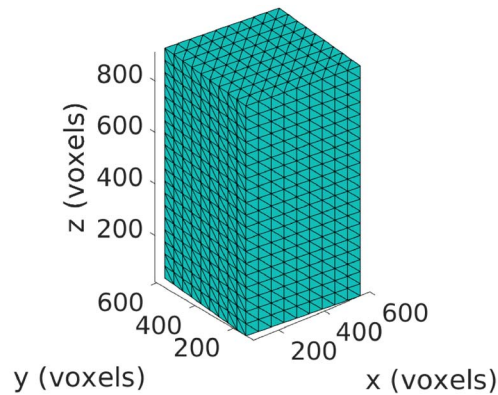
Figure 5. Mesh in the reference configuration consisting of 9234 T4 elements. The size of the analyzed region of interest is $480 \times 470 \times 893$ vx (or $19.8 \times 19.4 \times 38.4$ mm).

Table 2. DVC analysis parameters

DIC software	Correli 3.0 [34]
Image filtering	None
Element length (mean)	28 vx
Shape functions	linear (T4 elements [25])
Mesh	See Figure 5
Matching criterion	Sum of squared differences
Interpolant	Cubic
Displacement noise floor (vx)	0.06/0.05/0.04
Strain noise floor	$10^{-3}/10^{-3}/4 \times 10^{-4}$
	$5 \times 10^{-4}/3 \times 10^{-4}/4 \times 10^{-4}$
Principal strain noise floor	$1.3 \times 10^{-4}/4 \times 10^{-4}/4 \times 10^{-4}$

3.2. *Mesoscale DVC calculations*

DVC analyses were run directly for the three deformed scans using the backtracked mesh (Figure 5). The reconstructed volumes were registered using the Correli 3.0 framework [34]. The uncertainty quantification to evaluate the noise floor levels was based on the two scans of the reference configuration. A DVC analysis was run between these two volumes. Rigid body motions were subtracted from the measured displacement field, and the standard deviation of each nodal displacement component was estimated, and is reported in Table 2. Rather low levels were observed (i.e., 0.04–0.06 vx) thanks to the natural contrast of teak (Figure 1). For the strain components, their standard uncertainties were less than or equal to 10^{-3}, whereas the corresponding uncertainties for the principal strains varied from 4×10^{-4} to 1.3×10^{-3}. Even though the imaged material was very anisotropic in terms of correlation radii (Table 1) and contrast (Figure 1), it led to similar displacement and strain uncertainties at the mesoscale.

The DVC calculations were stopped when the L2-norm of displacement corrections were less than 10^{-3} vx. All direct calculations converged. The raw results were the displacement fields for the three angular amplitudes (Figure 6). For the first angular amplitude, the in-plane displacement fields have a different pattern as for the subsequent ones. It corresponds to the settling of the sample in the grips (Figure 2(a)), which explains the early nonlinear part of the torque vs. applied angular amplitude (Figure 3(a)). For the last angular amplitude, the longitudinal displacement field has more localized features along two vertical planes.
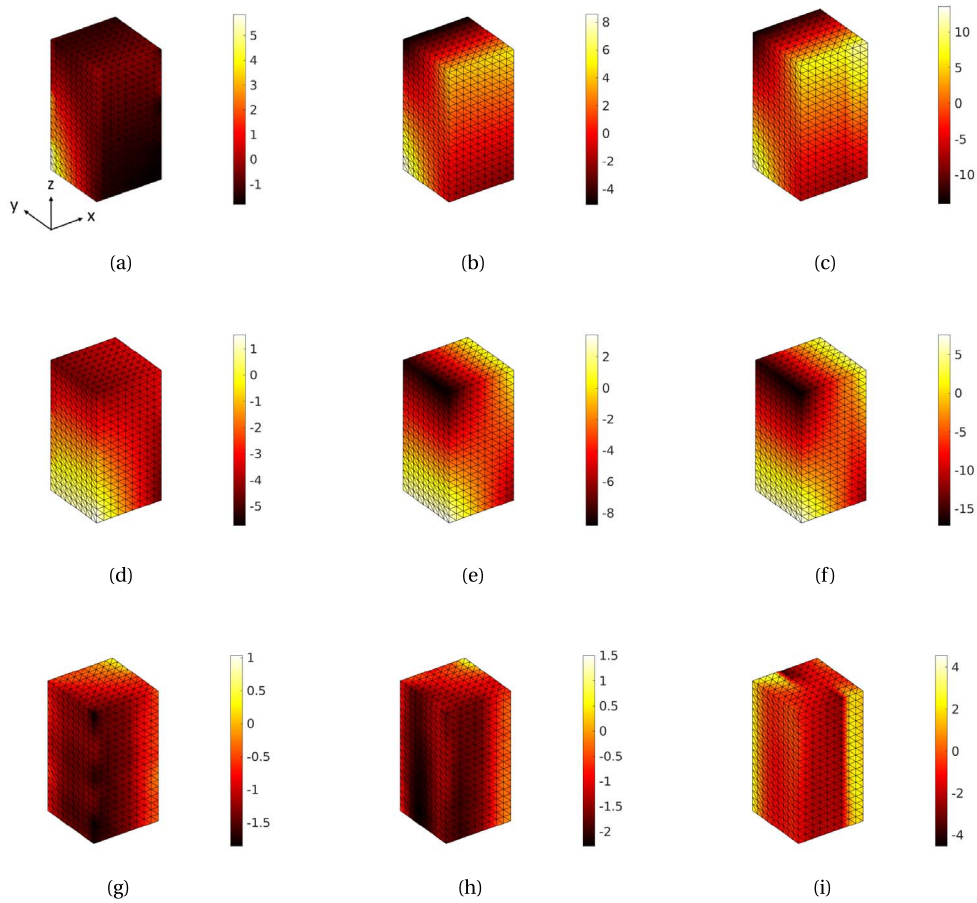
Figure 6. Measured displacement fields (expressed in vx) in the *x*-direction (a–c), *y*-direction (d–f), *z*-direction (g–i), for an angular amplitude of 5° (a,d,g), 10° (b,e,h), 15° (c,f,i).

To further investigate this last phenomenon, the voxel-wise gray level residuals are displayed in Figure 7 when thresholded between 10 and 30 gray levels. They consist of the gray level difference for any voxel in the region of interest of the reference configuration and of the deformed configuration corrected by the measured displacement [35]. The minimum level corresponds to twice the average level reached when registering the repeated scans in the reference configuration. The fact that the residual distribution did not reveal any particular feature proves that the registrations were successful for the first two angular amplitudes (Figure 7(a,b)). For the third amplitude, the registration was overall trustworthy as well, except in two regions of higher levels (Figure 7(c)). These zones coincide with higher longitudinal displacement gradients (Figure 6(i)). These two pieces of information prove that two cracks initiated and propagated between the second and third angular amplitudes, which was expected from the torque vs. angular amplitude response (Figure 3(a)); the two major load drops may be their signature.

From these preliminary analysis, it was concluded that no visible signs were observed for the first two angular amplitudes. Conversely, the third angular amplitude led to a damaged sample with two longitudinal cracks.

From the measured displacement fields, the Green–Lagrange strain fields were computed from the deformation gradient tensor that was obtained from exact differentiation of the
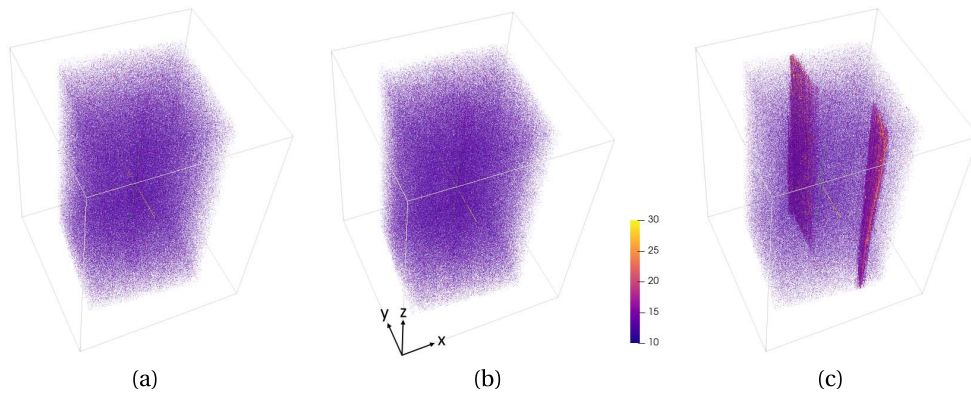
Figure 7. Gray level residuals for angular amplitudes of 5° (a), 10° (b), and 15° (c).
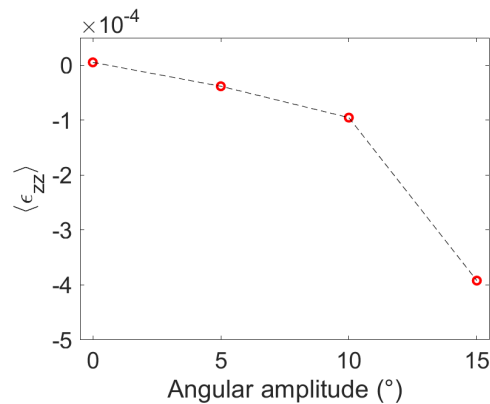

Figure 8. Mean longitudinal strain vs. angular amplitude.

T4 shape functions. An indirect way of evaluating Poynting effects is to analyze the mean longitudinal strain of the region of interest. Figure 8 shows the change of the latter with the applied angular amplitude. Even though limited, there was a clear shortening of the studied volume. Further, the Poynting effect became more pronounced once damage set in (for the last angular amplitude).

4. Analysis of damage

Three different scales of analysis were considered in this work. First, the macroscale corresponds to the region of interest of the sample that was analyzed via DVC (its size was 19.8 × 19.4 × 38.4 mm). Such a case was not investigated in previously reported DVC analyses on wood [18–20, 26,27]. Second, the mesoscale is related to the size of the finite elements used in the DVC analyses (i.e., 1.2 mm). The analyzed strain and crack opening displacement fields were assessed at that scale. Strain fields were reported at the same scale by Tran *et al.* [20]. Last, the microscale was that of the voxels of the reconstructed volumes, whose physical size was 43 μm. The registration quality was assessed at that scale (Figure 7), and corresponds to the so-called gray level residuals. Such residuals are very useful in detecting the presence of cracks [35, 36]. To the best of the authors' knowledge, no registration residuals were reported at that scale for wood.
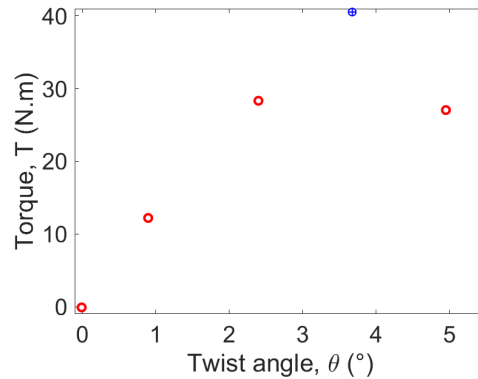
Figure 9. Torque vs. twist angle of the ROI analyzed via DVC. The blue reticle depicts the maximum torque (the twist angle is arbitrary).

4.1. *Macroscale results*

To study the macroscopic response of teak in torsion, the torque vs. twist angle was determined. Given the way the sample was gripped, the torque vs. angular amplitude plot (Figure 3(a)) could not be utilized. Instead, the twist angle θ was determined from DVC measurements. For the two end sections, their mean rotation along the longitudinal axis was assessed. The difference of these two quantities then corresponds to θ. Figure 9 shows the torque vs. twist angle response of the considered ROI. One additional (reticle) point was added to materialize the ultimate torque. However, since no tomographic acquisition was performed at that point, the twist angle is unknown.

To estimate the out-of-plane shear modulus of the studied material, the solution provided by the beam theory [37] was applied. The torque T versus twist angle θ relationship reads

$$T = G_z I_0 \frac{\theta}{L}, \tag{1}$$

where I_0 is the polar moment of inertia, L the length of the beam, and $G_z = G_{xz} = G_{yz}$ the out-of-plane shear modulus that was assumed to be identical for any in-plane direction. For solid rectangular sections (of width $2a$ and height $2b$), the polar moment of inertia reads

$$I_0 = ab^3 \left[\frac{16}{3} - 3.36 \left(\frac{b}{a} \right) \left(1 - \frac{b^4}{12a^4} \right) \right], \tag{2}$$

when $a \geq b$. In the present case, $2a = 19.8$ mm, $2b = 19.4$ mm and $L = 38.4$ mm. For the first angular amplitude, the mean torque during scan acquisition was equal to 12.3 N·m, and the corresponding twist angle was equal to 0.9°. Using Equation (1), the value of the out-of-plane shear modulus G_z was equal to 1.5 GPa, which is in very good agreement with the results reported by Hounlonon *et al.* [1] for the same type of wood.

For the second angular amplitude, the twist angle was equal to 2.4° and the corresponding torque was 28.4 N·m. The secant shear modulus was found equal to 1.3 GPa, which is 13% lower than its initial estimate. This result shows that even though there were no obvious mesoscopic (on the displacement fields) or microscopic (on the gray level residuals) signs, nonlinear phenomena had already set in.

The maximum shear stress $\tau_{\max}$, which corresponds to the maximum torque $T_{\max}$ (blue reticle in Figure 9), reads [37]

$$\tau_{\max} = \frac{3T_{\max}}{8ab^2} \left[1 + 0.61 \left(\frac{b}{a} \right) + 0.89 \left(\frac{b}{a} \right)^2 - 1.80 \left(\frac{b}{a} \right)^3 + 0.91 \left(\frac{b}{a} \right)^4 \right] \tag{3}$$
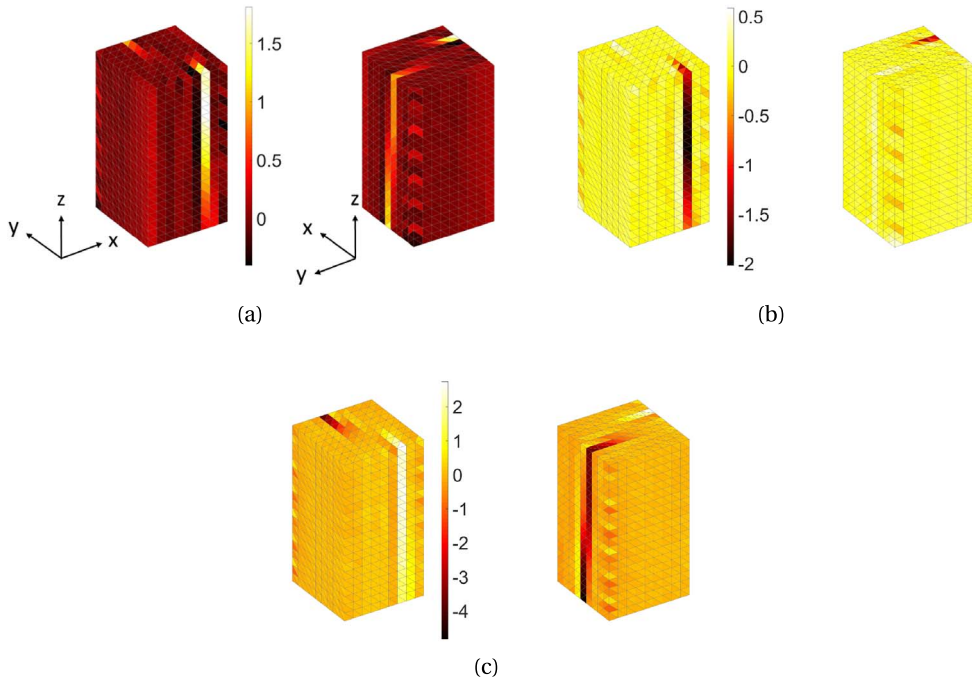
Figure 10. 3D renderings of the crack opening displacement fields (expressed in vx) $[\![u]\!]_{\mathrm{I}}$ (a), $[\![u]\!]_{\mathrm{II}}$ (b), and $[\![u]\!]_{\mathrm{III}}$ (c) for the last angular amplitude. For each sub-figure, views for two orientations are shown to analyze both cracks.

and was equal to 26.1 MPa ($T_{\max} = 40.5$ N·m). For the continuous test, the maximum torque was equal to 40.1 N·m, which led to an ultimate shear strength of 25.8 MPa.

The estimation of the shear modulus was not performed for the third angular amplitude since localized phenomena had already occurred (Figure 7(c)). The zones coincided with higher longitudinal displacement gradients (Figure 6(i)). More local analyses were called for.

4.2. Mesoscale studies

The mesoscale analyses corresponded to studying the strain fields, which are uniform over each element of length ℓ. As the mean torque level was very close for the last two angles of twist (Figure 9), it was possible to assess the regular (i.e., elastic) and singular (i.e., due to cracks) contributions to the strain tensor for the last angular amplitude. The normal to the crack planes was essentially aligned along the x-direction (Figure 7). The elastic part of the strain was assumed to be identical to the total strain of the second angular amplitude. Consequently, the strain increment between the second and third angular amplitudes corresponds to the contribution of average crack openings in modes I, II and III per element (i.e., $[\![u]\!]_{\mathrm{I}} = \delta\epsilon_{xx}\ell$, $[\![u]\!]_{\mathrm{II}} = 2\delta\epsilon_{xy}\ell$, and $[\![u]\!]_{\mathrm{III}} = 2\delta\epsilon_{xz}\ell$).

Figure 10 shows the three crack opening displacement fields. High levels of mode I crack opening displacements (CODs) are observed (Figure 10(a)), which indicate that there was a significant mode I contribution for one of the two cracks. The mode II contribution remained more modest for the second crack. Interestingly, the mode III contribution was the highest for the crack that experienced less CODs in modes I and II. Conversely, the other crack underwent
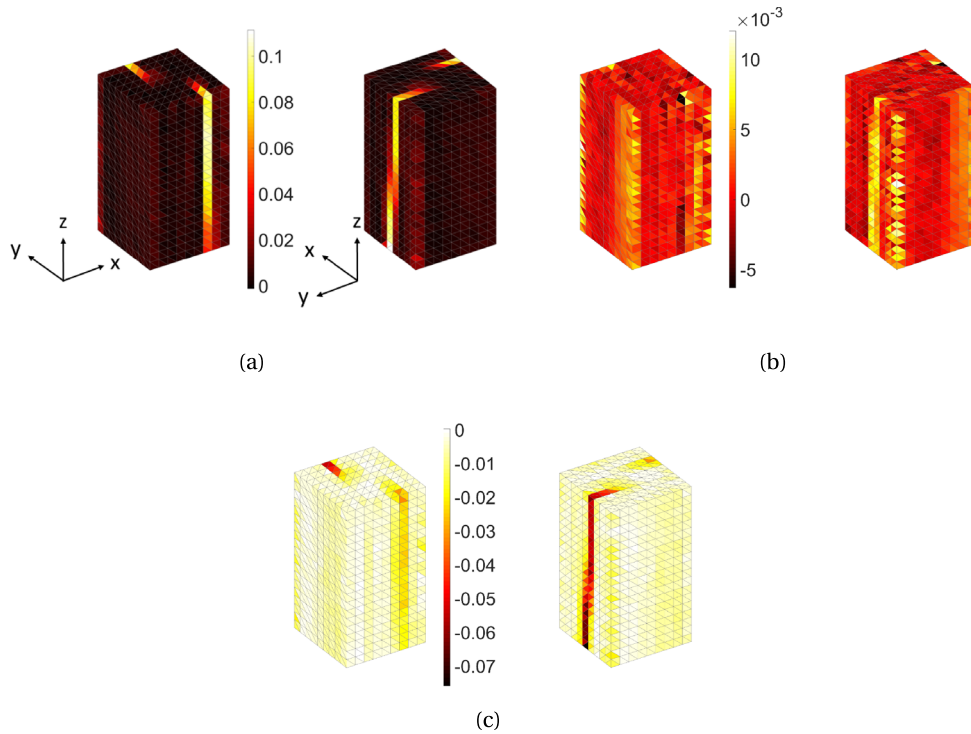
Figure 11. 3D renderings of principal strain increment fields $\delta\epsilon_1$, $\delta\epsilon_2$ and $\delta\epsilon_3$ for the last angular amplitude. For each sub-figure, views for two orientations are shown to analyze both cracks.

similar levels in all three modes. The present analysis shows that one crack was in fully mixed mode, whereas the other one was in a mode I/III regime with a dominant mode III contribution.

Figure 11 shows the three principal strain increment fields ($\delta\epsilon_1 \geq \delta\epsilon_2 \geq \delta\epsilon_3$) between the second and third angular amplitudes. It is worth noting that the second principal strain increment remained rather low in comparison with the other two components, even in the cracked region. This result indicates that the dominant strain components were $\delta\epsilon_{xx}$, $\delta\epsilon_{xy}$ and $\delta\epsilon_{xz}$, which would then lead to a vanishing principal strain increment $\delta\epsilon_2$. Further, there is a significant level of mode II and III CODs since the magnitude of $\delta\epsilon_3$ was high.

4.3. *Microscale investigations*

Last, the correlation residuals are studied. They were computed voxel-wise, and therefore the corresponding scale is that of each voxel whose physical size was 43 µm. The gray level residuals were further thresholded for the last loading amplitude (Figure 7(c)) in Figure 12(a) to better reveal the two cracks. Given the fact that these residuals were computed in the reference configuration, they were laid over the microstructure in the reference (i.e., undamaged) configuration (Figure 12(b)). It is observed that both cracks lie at growth interfaces, which are weak zones allowing cracks to propagate more easily.

The ring boundary visible on cross-sections of the sample is a zone of strong mechanical and anatomical contrast between winter wood for one ring and spring wood for the next ring. According to Hassel *et al.* [38], a thin region of low density near the late wood–early wood interfaces dominates the shear deformation in an annual ring, due to a strong correlation
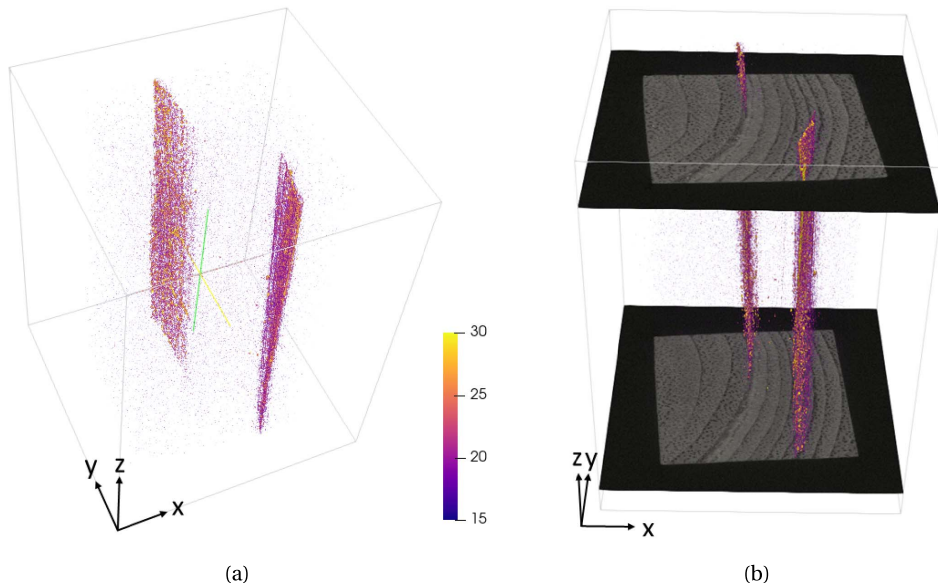
(a)   (b)

Figure 12. (a) Thresholded gray level residuals for the angular amplitude of 15° revealing the presence of two cracks. (b) Gray level residuals laid over two sections of the reference configuration.

between shear deformation and density. Spring wood is often less dense than summer wood. Therefore a mechanical anisotropy at the scale of the growth layer exists, which is attributed to the presence of these two physiologically specific tissues (early and late wood) [39–41]. This intra-ring variability was confirmed by Simon [12] who reported a sudden change of shear modulus at the microscale that may cause cracking at the boundary of annual rings.

5. Conclusion

An *in situ* torsion test was carried out on Beninese teak wood. A dwell time of 5 min was performed before each acquisition to mitigate stress relaxation. Thanks to the contrast of the imaged wood at the microscale, DVC analyses were run using the reconstructed volumes for different angular amplitudes. Rather low and isotropic measurement uncertainties were found even though the underlying contrast was anisotropic. The feasibility of *in situ* torsion tests on wood and their quantitative analyses via DVC were therefore validated.

From a macroscopic point of view, the out-of-plane shear modulus and ultimate shear strength of teak could be estimated. The level of shear modulus was in good agreement with reported values for the studied wood. It was also shown that damage had set in for an applied torque equal to 75% of the ultimate load (i.e., a degradation of 13% of the initial Young's modulus). For the third analyzed load step (i.e., beyond the ultimate load), macroscopic damage had occurred in the form of two longitudinal cracks.

Thanks to the strain and crack opening displacement fields estimated at a mesoscale, it was shown that both cracks experienced mixed mode propagation. It was also checked that the dominant shear deformation of the studied wood was in the radial and tangential directions. The analysis of the correlation residuals at the microscale showed that the cracks were perpendicular to the growth (radial) direction along interfaces between early and late wood, namely, where there was mechanical anisotropy and contrast at the growth rings.

Conflicts of interest

The authors declare no competing financial interest.

Dedication

The manuscript was written through contributions of all authors. All authors have given approval to the final version of the manuscript.

Acknowledgments

References

[1] M. Hounlonon, C. Kouchadé, B. Kounouhewa, "Propriétés physiques et mécaniques du bois de teck de provenances tanzanienne et locale au Bénin", *Bois et Forêts des Trop.* **331** (2017), no. 1, p. 45-63.

[2] D. Louppe, A. Oteng-Amoako, M. Brink, *Tectona grandis L.f.*, PROTA, Wageningen, Netherlands, 2005.

[3] NF B 51-003, *Caractérisation des propriétés mécaniques du bois*, AFNOR – Association française de normalisation, 1942.

[4] A. D. Kokutse, K. Adjonou, K. Kokou, M. Gbeassor, "Problématique de la qualité du teck de provenance tanzanienne par rapport au teck local en plantation au Togo", *Bois et Forêt des Trop.* **302** (2009), p. 43-52.

[5] I. Miranda, V. Sousa, H. Pereira, "Wood properties of teak (*Tectona grandis*) from a mature unmanaged stand in East Timor", *J. Wood Sci.* **57** (2011), p. 171-178.

[6] P. Thulasidas, K. Bhat, "Mechanical properties and wood structure characteristics of 35-year old home-garden teak from wet and dry localities of Kerala, India in comparison with plantation teak", *J. Indian Acad. Wood Sci.* **9** (2012), p. 23-32.

[7] D. Rizanti, W. Darmawan, B. George, A. Merlin, S. Dumarcay, H. Chapuis, C. Gérardin, E. Gelhaye, P. Raharivelomanana, R. Sari, W. Syafii, R. Mohamed, P. Gerardin, "Comparison of teak wood properties according to forest management: short versus long rotation", *Ann. For. Sci.* **75** (2018), article no. 39.

[8] Y. Ramasamy, E. Galeano, T. Win (eds.), *The Teak Genome, Compendium of Plant Genomes*, Springer Nature, Cham, Switzerland, 2021.

[9] J. Prezelj, A. Nikonov, I. Emri, "Using sound in the very near field of vibrating plates for determination of their mechanical properties", *Appl. Acoust.* **186** (2022), article no. 108486.

[10] A. A. française de normalisation, "NF B 51-012, Bois – Essai de cisaillement", 2019.

[11] M.-T. Gautherin, "Critère de contrainte limite du bois massif", PhD Thesis, Université Pierre et Marie Curie, Paris 6, 1980 (in French).

[12] P. Simon, "Approche multiéchelle du comportement mécanique du bois dans le plan transverse", PhD Thesis, Institut National des Sciences Appliquées de Lyon, 2009 (in French).

[13] R. Keller, C. Millier, "Use of density components in xylochronology", *Ann. For. Sci.* **27** (1970), no. 2, p. 157-196.

[14] J. Bodig, J. Goodman, "Prediction of elastic parameters for wood", *Wood Sci.* **5** (1973), no. 4, p. 249-264.

[15] D. Guitard, *Mécanique du matériau bois et composites*, Cepadues, Toulouse, France, 1987.

[16] B. Zobel, J. Buijtenen, *Wood Variations, its Causes and Control*, Springer Verlag, Berlin, Germany, 1989.

[17] M. C. Trouy, P. Triboulot, *Matériau bois – Structure et caractéristiques*, vol. C925, Techniques de l'ingénieur, Saint-Denis, France, 2001.

[18] F. Forsberg, R. Mooser, M. Arnold, E. Hack, P. Wyss, "3D micro-scale deformations of wood in bending: Synchrotron radiation μCT data analyzed with digital volume correlation", *J. Struct. Biol.* **164** (2008), p. 255-262.

[19] F. Forsberg, M. Sjödahl, R. Mooser, E. Hack, P. Wyss, "Full three-dimensional strain measurements on wood exposed to three-point bending: Analysis by use of digital volume correlation applied to synchrotron radiation micro-computed tomography image data", *Strain* **46** (2010), no. 1, p. 47-60.

[20] H. Tran, P. Doumalin, C. Delisée, J. Dupré, J. Malvestio, A. Germaneau, "3D mechanical analysis of low-density wood-based fiberboards by X-ray microcomputed tomography and Digital Volume Correlation", *J. Mater. Sci.* **48** (2012), p. 3198-3212.

[21] M. Sutton, "Computer vision-based, noncontacting deformation measurements in mechanics: A generational transformation", *Appl. Mech. Rev.* **65** (2013), no. AMR-13-1009, article no. 050802.

[22] B. Bay, T. Smith, D. Fyhrie, M. Saad, "Digital volume correlation: three-dimensional strain mapping using X-ray tomography", *Exp. Mech.* **39** (1999), p. 217-226.

[23] B. Bay, "Methods and applications of digital volume correlation", *J. Strain Anal. Eng. Des.* **43** (2008), p. 745-760.

[24] S. Roux, F. Hild, P. Viot, D. Bernard, "Three dimensional image correlation from X-ray computed tomography of solid foam", *Compos. Part A Appl. Sci. Manuf.* **39** (2008), no. 8, p. 1253-1265.

[25] F. Hild, A. Bouterf, L. Chamoin, F. Mathieu, J. Neggers, F. Pled, Z. Tomičević, S. Roux, "Toward 4D Mechanical Correlation", *Adv. Model. Simul. Eng. Sci.* **3** (2016), no. 1, p. 1-26.

[26] C. El Hachem, K. Abahri, R. Bennacer, "Original experimental and numerical approach for prediction of the microscopic hygro-mechanical behavior of spruce wood", *Constr. Build. Mater.* **203** (2019), p. 258-266.

[27] J. Carlsson, M. Heldin, P. Isaksson, U. Wiklund, "Investigating tool engagement in groundwood pulping: finite element modelling and in-situ observations at the microscale", *Holzforschung* **74** (2020), no. 5, p. 477-487.

[28] E. Maire, P. J. Withers, "Quantitative X-ray tomography", *Int. Mater. Rev.* **59** (2014), no. 1, p. 1-43.

[29] J. Buffière, E. Maire, J. Adrien, J. Masse, E. Boller, "In situ experiments with X ray tomography: an attractive tool for experimental mechanics", *Exp. Mech.* **50** (2010), no. 3, p. 289-305.

[30] E. Schwab, P. Polaczek, "Bestimmung der Schubmoduln von Holz durch statische Torsionsversuche Beitrag zur Neufassung DIN 52190", *Holz Roh Werkst.* **35** (1977), p. 23-27.

[31] J. Poynting, "XXXIX. Radiation pressure", *Lond. Edinb. Dublin Philos. Mag. J. Sci.* **9** (1905), no. 52, p. 393-406.

[32] L. Feldkamp, L. Davis, J. Kress, "Practical cone beam algorithm", *J. Opt. Soc. Am.* **A1** (1984), p. 612-619.

[33] P. Auger, T. Lavigne, B. Smaniotto, M. Spagnuolo, F. dell'Isola, F. Hild, "Poynting effects in pantographic metamaterial captured via multiscale DVC", *J. Strain Anal. Eng. Des.* **56** (2021), no. 7, p. 462-477.

[34] H. Leclerc, J. Neggers, F. Mathieu, F. Hild, S. Roux, *Correli 3.0. IDDN.FR.001.520008.000.S.P.2015.000.31500*, Agence pour la Protection des Programmes, Paris, France, 2015.

[35] F. Hild, A. Fanget, J. Adrien, E. Maire, S. Roux, "Three dimensional analysis of a tensile test on a propellant with digital volume correlation", *Arch. Mech.* **63** (2011), no. 5–6, p. 1-20.

[36] F. Hild, A. Bouterf, S. Roux, "Damage measurements via DIC", *Int. J. Fract.* **191** (2015), no. 1-2, p. 77-105.

[37] W. C. Young, R. G. Budynas, *Roark's Formulas for Stress and Strain*, 7 ed., McGraw-Hill, New York, USA, 2001, Ch. 10, 401 pages.

[38] B. Hassel, C. Modén, P. Berard, L. Berglund, "Single cube apparatus - Shear properties determination ans shear strain variation in natural density gradient materials", in *ICCM-17 17th International Conference on Composite Materials*, 2009, http://urn.kb.se/resolve?urn=urn:nbn:se:kth:diva-152372.

[39] A. Ylinen, P. Jumppanen, "Theory of the shrinkage of wood", *Wood Sci. Technol.* **1** (1967), p. 241-252.

[40] J. Dumail, "Caractéristiques physiques et mécaniques du bois juvénile de pin maritime (Pinus pinaster)", PhD Thesis, Université Bordeaux 1, 1995 (in French).

[41] F. Farruggia, "Détermination du comportement élastique d'un ensemble de fibres de bois à partir de son organisation cellulaire et d'essais mécaniques sous microscope", PhD Thesis, ENGREF Nancy, 1998 (in French).